Ultrasonics 141 (2024) 107332

Contents lists available at ScienceDirect

Ultrasonics

journal homepage: www.elsevier.com/locate/ultras

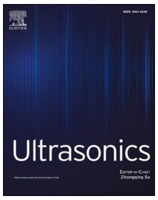

Investigation of 3D vessel reconstruction under Doppler imaging with phantoms: Towards reconstruction of the Circle of Willis

Shuai Li [a], Queenie Tsung Kwan Shea [a], Yan To Ling [a,c], Yong-Ping Zheng [a,b,*]

[a] Department of Biomedical Engineering, The Hong Kong Polytechnic University, Hong Kong Special Administrative Region, China
[b] Research Institute of Smart Ageing, The Hong Kong Polytechnic University, Hong Kong Special Administrative Region, China
[c] Centre for Developmental Neurobiology, Institute of Psychiatry, Psychology and Neuroscience, King's College London, London, United Kingdom

ARTICLE INFO

Keywords:
Stroke
Circle of Willis
Brain
Ultrasound imaging
3D ultrasound
Doppler imaging

ABSTRACT

Background: Stroke is the second leading cause of death across the globe. Early screening and risk detection could provide early intervention and possibly prevent its incidence. Imaging modalities, including 1D-Transcranial Doppler Ultrasound (1D-TCD) or Transcranial Color-code sonography (TCCS), could only provide low spatial resolution or 2D image information, respectively. Notably, 3D imaging modalities including CT have high radiation exposure, whereas MRI is expensive and cannot be adopted in patients with implanted devices. This study proposes an alternative imaging solution for reconstructing 3D Doppler ultrasound geared towards providing a screening tool for the 3D vessel structure of the brain.

Methods: The system comprises an ultrasound phased array attached to a servo motor, which can rotate 180° at a speed of 2°/s. We extracted the color Doppler ROI from the image before reconstructing it into a 3D view using a customized pixel-based algorithm. Different vascular diameters, flow velocity, and depth were tested using a vascular phantom with a pumped flow to confirm the system for imaging blood flow. These variables were set to mimic the vessel diameter, flow speed, and depth of the Circle of Willis (CoW) during a transcranial screening.

Results and conclusions: The lower values of absolute error and ratio were found in the larger vascular channels, and vessel diameter overrepresentation was observed. Under different flow velocities, such diameter overrepresentation in the reconstructed flow did not change much; however, it did change with different depths. Meanwhile, the setting of the velocity scale and the color gain affected the dimension of reconstructed objectives. Moreover, we presented a 3D image of CoW from a subject to demonstrate its potential. The findings of this work can provide a good reference for further studies on the reconstruction of the CoW or other blood vessels using Doppler imaging.

1. Introduction

Stroke is the second-leading cause of death, causing an annual estimate of 12.2 million cases and 6.55 million mortalities globally [1]. In China, stroke causes approximately 1.6 million deaths annually, causing an enormous economic and social burden on society [2]. Stroke is a result of blood supply interruption to the brain, followed by the death of brain cells due to the lack of oxygen supply. The reasons for interruption can be classified into blockage and rupture of blood vessels, including ischemic and hemorrhagic stroke, respectively [3]. Early stroke prediction is essential considering that an estimated 85 % of strokes cause death and severe/moderate disability [4]. Although the cause of stroke is multifactorial and could be related to age, gender, race, family, medication, high blood pressure, smoking, heart disease, and diabetes [3], most symptoms of stroke are linked to the cerebral arteries [5]. Among the cerebral arteries, there is a key anatomical structure called the Circle of Willis (CoW), which includes middle cerebral arteries (MCAs), internal carotid arteries (ICAs), anterior cerebral arteries (ACAs), posterior cerebral arteries (PCAs), posterior communicating arteries (PCoAs), and anterior communicating artery (ACoA).

Thomas Wills first described the CoW in 1664 [6], and its role is to maintain cerebral blood flow to the brain even if occlusion or stenosis occurs in one of the cerebral arteries [7]. The pressure from blockage may alter the direction of blood flow forward or backward; this enables the flow to reach similar brain structures. However, variants/incompleteness of the CoW are common and only 21 % of individuals had a

---

* Corresponding author.
E-mail address: yongping.zheng@polyu.edu.hk (Y.-P. Zheng).

https://doi.org/10.1016/j.ultras.2024.107332
Received 21 May 2023; Received in revised form 26 September 2023; Accepted 23 April 2024

complete CoW in 1998 [8]. Another study revealed that only 34.5 % of cases were detected with classic anatomy of CoW in 1413 brains [9]. However, some studies reported a significant percentage of incomplete CoW ranging from 50-80 % in different countries [10–16]. Meanwhile, a few types of variants were associated with both hemorrhage and ischemic stroke [17–21]. Detecting the structural and hemodynamic changes in the CoW plays a significant role in stroke screening, hence minimizing the risk of stroke events.

Due to its benefits of real-time captures of both structural and hemodynamic information in the CoW, transcranial color-code sonography (TCCS), also known as transcranial color-code Doppler (TCCD), is clinically used for stroke screening. Also, the benefits of non-invasiveness, free radiation, and low cost make TCCS indispensable compared to other common imaging modalities, including computed tomography angiography (CTA) and magnetic resonance angiography (MRA) [22–24]. TCCS is performed using a phased array transducer to capture the inside of the skull through acoustic bone windows, including the orbital window, temporal window, and occipital window [25]. The color mode for TCCS is color flow imaging (CFI), indicating a frequency change of the Doppler signal. In contrast, color power imaging (CPI) represents the amplitude change of the Doppler signal [26].

However, the TCCS is hindered by the lack of spatial information and relatively low anatomical accuracy, unlike CTA and MRA. In the last decades, a 1D phased array transducer with mechanical methods of tilting scanning [27–31] or a 2D array transducer [32,33] has been developed to make TCCS into a 3-D level. The color modes used in these two techniques include CFI and CPI, respectively; this work called them 3D-CFI via 2D transducer and 3D-CPI for easy understanding. These 3D techniques are directly applied to human subjects by measuring the detection rate of cerebral vessels. Although 3D-CPI reported a good outcome of average detection rate, improving from 60 % to 90 % by injecting the contrast agent, hemodynamic information without flow direction would limit its clinical application. Regarding 3D-CFI via the 2D transducer, the hemodynamic information can be successfully captured but only approximately 60 % of the average enhanced detection rate can be found. Thus, the three-dimensional TCCS urgently needs high Doppler sensitivity and good completeness of hemodynamic information.

Additionally, the anatomical accuracy presented in TCCS is a huge challenge due to color overrepresentation; this is possibly caused by the complex transmission path of ultrasound inside of the skull and greater Doppler signal from relatively high-speed blood flow in small cerebral vessels. The interdependent or independent factors, including imaging depth, transducer frequency, velocity scale, color gain, pulse repetition frequency, frame rate, and depth of Doppler interrogation, among others [34], can influence this overrepresentation; however, the use of these controls and subsequent changes in the color maps vary from device to device. Moreover, it is difficult to adjust all these factors in TCCS due to non-visualized vessels in B-mode and one customized setting of parameters to simultaneously display multiple vessels. Therefore, the setting of velocity scale and color gain are acceptable for adjustment to ensure imaging adequacy of TCCS in commercial ultrasound imaging equipment and easy operation. Meanwhile, a larger color overrepresentation is delivered in CFI because of poor noise containment unlike CPI [26]. An overrepresentation would also happen in the 3D view; however, no quantitative analysis was conducted in these studies.

This work introduced a novel imaging system for transcranial 3D color Doppler. A single-crystal phased array transducer was used to improve the Doppler sensitivity. Further, an advanced mode of directional CPI (dCPI) was used to combine the enhanced sensitivity of CPI with the directional information of CFI [35]. For a more complete imaging view, the mechanical method of rotating scanning was applied for data acquisition rather than tilting scanning. Moreover, the system was validated by investigating the extent to which the factors, including Doppler interrogation depth, vascular diameter, flow velocity, and settings of color gain and velocity scale, influenced color overrepresentation on 3D display. The quantitative analysis could be a key reference for our further human research and provide future inspiration on how to calibrate the overrepresenting factors.

2. Methods

The 3D ultrasound imaging system included the hardware and software components. The hardware part was used to collect ultrasound color images for further 3D reconstruction. On the other hand, the software part was used to develop imaging processing methods and an algorithm for 3D reconstruction.

2.1. Hardware design

Fig. 1 shows the diagram of the hardware part, which includes ultrasound imaging equipment and a rotating probe carrier as the primary components. The ultrasound probe of the equipment was clamped on top of the rotating probe carrier. Scanning was performed using ultrasound imaging equipment (Aixplorer model, SuperSonic Imagine, France) with a single-crystal phased array ultrasound probe (XP5-1, 96 transducer elements and 1–5 MHz of bandwidth). The relatively low-frequency range ensured ultrasound penetration through the skull. The rotating probe carrier comprised a single-chip microcontroller (Arduino Uno, Italy), a servo motor (LX-225 model, Hiwonder, China), and a motor driver module. The motor carried the ultrasound probe, rotating it clockwise for 180 degrees. The accuracy of the servo motor was 0.24° as a default setting, and the frame rate of ultrasound imaging equipment was 11 Hz. For adequate slices of 3D reconstruction, the microcontroller was programmed to control the servo motor using a rotating speed of 2 deg/sec. Thus, more than 900 slices were collected for 3D reconstruction. The Arduino Uno communicated with the servo motor through the motor driver, as all the complied commands of control were integrated into the motor driver module. To access the motor driver module, a program library called LobotServiController (downloaded from GitHub) was added to the Arduino Integrated Development Environment (IDE), as all Arduino codes were conducted on the Arduino IDE. Arduino Uno controlled the motor driver module via serial communication with a baud of 115,200 for motor rotation. Meanwhile, the position information, including the rotated time and angle of the servo motor was sent back to the microcontroller. Regarding image data collection, a video capture card was used to collect ultrasound color Doppler images by recording the displayed ultrasound images. We used directional color power imaging (dCPI) color mode, which is an advanced imaging mode integrating enhanced sensitivity of CPI with the directional information of CFI [35]. A rechargeable lithium battery was used to power the rotating probe carrier.

2.2. Software design

Two applications were developed for data collection and 3D reconstruction, respectively. Both were constructed using an IDE of Microsoft Visual Studio (VS) using C++ language. The application of data collection was to record ultrasound Doppler images and trigger the rotation of the probe carrier simultaneously. The COM port connecting to Arduino Uno would be turned on and send the command of rotation once the capture card started to capture the ultrasound image. All the captured images were formed into a video file in AVI format, and the position information was saved in a txt file.

Fig. 2 shows the set of image processing methods. In the 3D reconstruction, the 2D image data within the Doppler ROI was converted into a 3D space. ROI, the color area, was extracted using a set of image processing methods. The raw image was converted from RGB level to gray level first; the connected-component labeling was then used to remove the labels, color bar, and machine logo from the image. The remaining B-mode ultrasound grayscale had the same red, green, and blue values in the decimal code of the RGB level. Thus, removing the

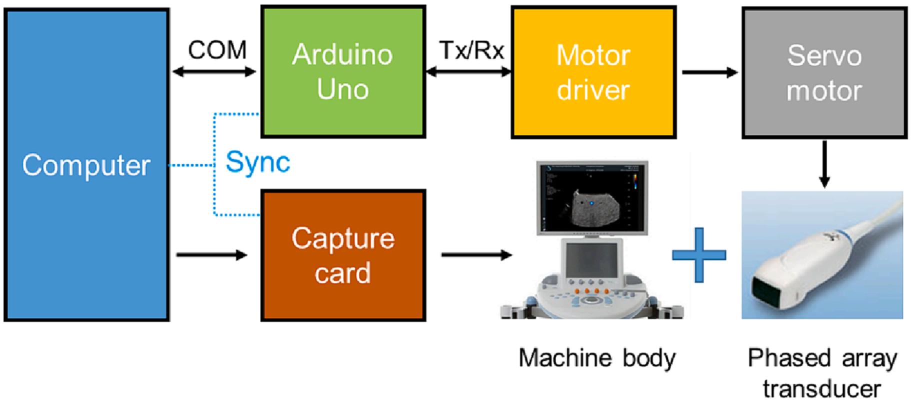

Fig. 1. The diagram showing the hardware part, COM port refers to the communication port between computer and microcontroller. Tx/Rx represents the serial communication between microcontroller and motor driver.

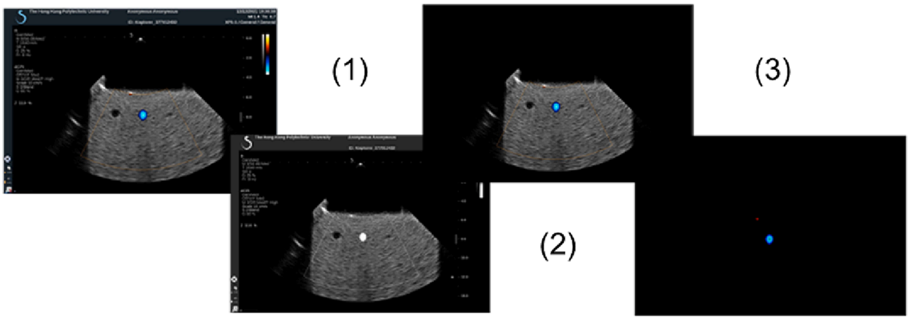

Fig. 2. An illustration of image processing methods. Step (1) involves the conversion of the raw image from RGB level to gray level; step (2) aims to retain useful information in the image; step (3) involves the remove B-mode background and the fan-shaped outline.

background B-mode images (grays) was efficiently performed by subtracting the minimum of the decimal coded values. However, it could also remove the white color from a high-flow velocity region, since a high-velocity region only exists at the center of the vessel, the white color could be refilled into the center of the vessel by identifying the vessel outline. Meanwhile, noises, including the fan-shaped outline, can be eliminated by morphological opening.

After obtaining the ROI from each ultrasound Doppler image, the pixels in a 2-dimensional image were mapped to voxels in a 3D view using a customized pixel-based algorithm. The revolution axis of the rotating probe carrier was designed to match the middle line of images. The size of each image was 1535*1080 (x, y), equivalent to a resolution of 1.80 mm per pixel. To make the coordinates of all points always positive, the origin was located at the bottom left corner, and the axis of rotation was the middle line of the images. Thus, the maximum dimension of the voxels was 1535*1080*1535 (Nx*Ny*Nz). The customized equations of transfer quoted the rotation matrix on the y-axis as shown below (1)-(6), where θ represents the rotated angle; X, Y, and Z indicate the coordinate of the voxel; x and y indicate the coordinate of the pixel; w is the width of the image. Y would be kept the same as y since the rotating axis is parallel to the y-axis, and the Z would be fixed at w/2 at the initial angle.

If $\theta \leq 90^\circ$:

$$X = x^*cos(\theta) + w^*(1 - cos(\theta))/2 \tag{1}$$

$$Y = y \tag{2}$$

$$Z = x^*sin(\theta) + w^*(1 - sin(\theta))/2 \tag{3}$$

If $\theta > 90^\circ$:

$$X = w/2 - (x - w/2)^*cos(\pi - \theta) \tag{4}$$

$$Y = y \tag{5}$$

$$Z = (x - w/2)^*sin(\pi - \theta) + w/2 \tag{6}$$

In these applications, an open-source computer vision library (OpenCV) was used to process images. The Visualization Toolkit (VTK) was used to construct and display the 3D view by creating a point cloud, comprising more than 0.9 million points. The user interface (UI) was developed by adding a widget toolkit (Qt). Fig. 3 shows the reconstructed objective and the user interface.

2.3. Experimental setup

Considering that the system aimed to build a 3D view of blood flow, we developed a setup for generating liquid flow to verify the system but without pulsation, as shown in Fig. 4. In this test, a peristaltic pump (Masterflex L/S, Germany) was utilized to pump fluid at a constant volume speed, but it could be adjusted by increasing or decreasing the value of revolutions per minute (rpm). Next, the flow passed a flowmeter (Gilmont Accucal, Germany) before entering the vascular phantom (ATS-524, CRIS, USA), and the flowmeter was used as a reference for indicating the volumetric flow rate. The vascular phantom was placed inside a water-filled tank because it could easily change the angle and distance while maintaining consistent coupling. Subsequently, the flow was redirected back to the peristaltic pump, completing a loop. Throughout the data collection process, the top of the phased-array probe was submerged in water, positioned at a 30° angle towards the vascular phantom. Following this, the probe carrier rotated the phased array probe clockwise by 180°, capturing ultrasound Doppler images concurrently.

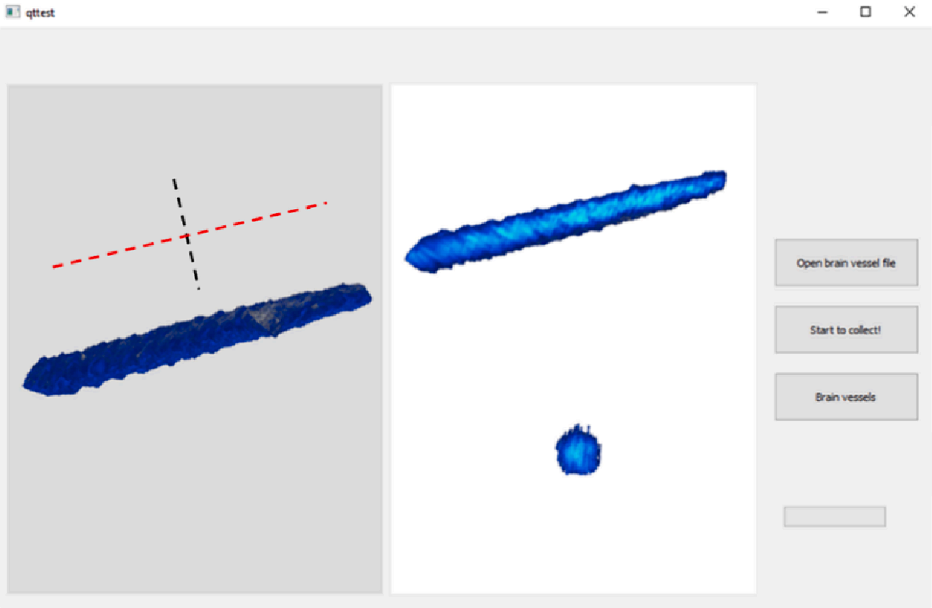

Fig. 3. The user interface can display the constructed objective in different cross-sectional views; sectional planes are indicated by the black and red dash lines. (For interpretation of the references to color in this figure legend, the reader is referred to the web version of this article.)

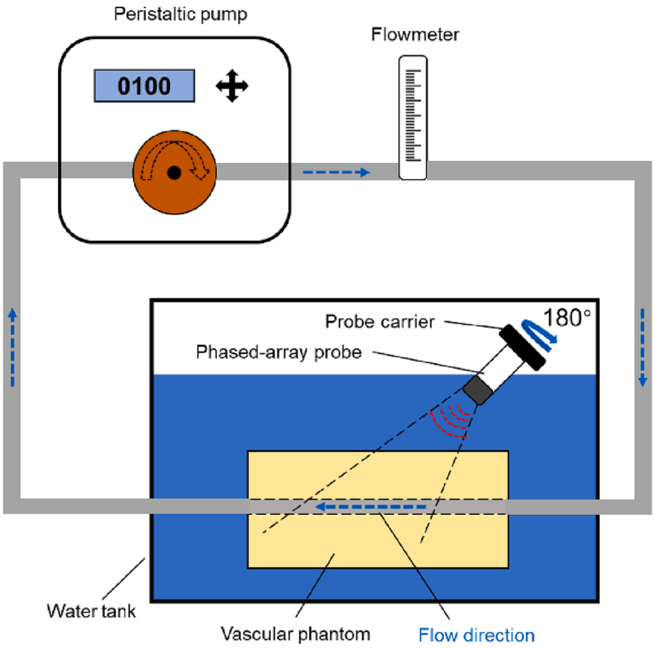

Fig. 4. The experimental setup for system verification.

2.4. Variables for verification and some measurements

In this study, three variables were investigated: vascular diameter, flow velocity and depth between ultrasound probe and the vessel. The vascular phantom contained four channels, with corresponding diameters of 2, 4, 6 and 8 mm, respectively. Given that the diameter of the terminal ICA can reach up to 4.6 mm [36], channels of 2, 4, and 6 mm in diameter were employed to validate the system. The average of blood flow velocity in CoW covered a wide range from 36 ± 12 cm/s to 62 ± 12 cm/s [37,38]. Hence, we postulated that the flow velocities of approximately 20–50 cm/s in different diameter channels were aimed at mimicking the blood velocity in cerebral arteries. The rpm setting of the peristaltic pump showed the capacity to control flow velocity, and the rpm values are shown in Table 1. Simultaneously, the flow velocity was assessed using pulse-wave Doppler mode, with measurements taken at the proximal, middle, and distal sections of the vascular channel, and a mean value was calculated. It's worth noting that, in addition to flow velocity, the adjustment of the speed scale may impact the pulse repetition frequency (PRF), consequently altering the range of velocities represented in the image. Two groups were used to determine the effect of the speed scale: the matching scale and the constant scale. The matching scale indicated that the value of the speed scale was set close to the pumped flow velocity, while the constant scale maintained a fixed speed scale which was only set close to the minimal pumped flow velocity.

Moreover, three depths of 30 mm, 60 mm, and 90 mm were established to mimic the location of arteries in CoW because these arteries were located at approximately a depth of 30 mm to 80 mm depth from the temporal window [39].

2.5. Data analysis and statistics

All data were converted into a suitable format using a custom script written in MATLAB (MathWorks Inc., Natick, MA, USA). All statistical analyses were conducted using GraphPad Prism (GraphPad Software Inc., LaJolla, CA, USA). To quantify the dimension of the reconstructed objectives, at least 100 slices were employed to imitate circles (Fig. 5). Next, the mean value of the diameter was calculated from all the imitated circles, and the average value was defined as the reconstructed diameter. To analyze the dimensional changes in the reconstructed

Table 1
The rpm setting for different vascular diameters.

Diameter (mm)	Flow velocity (cm\s)	rpm setting
6	21.42	57
	31.29	103
	42.18	132
	50.26	188
4	20.33	28
	29.67	52
	38.91	61
	50.24	84
2	52.78	27

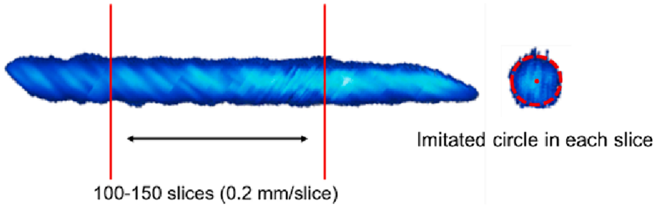

Fig. 5. 100 to 150 slices shown in the middle part of the reconstructed objective were used to calculate the average diameters of the imitated circles.

objects, we computed the absolute error and the ratio of the reconstructed diameter to the actual diameter for comparison. The significance of any differences was assessed using a *t*-test.

2.6. Demonstration of 3D CoW reconstruction

The imaging system was applied to a human subject by locating the phased array transducer at one lateral side of the temporal window. Here, it was the right side. The data collection initiated when ACAs, PCAs, and MCAs could be seen on the interrogating window. Subsequently, processing and reconstruction were performed to demonstrate a 3D view of the CoW.

3. Results

3.1. Reconstruction under different vascular diameters

A mean flow velocity of approximately 50 cm/s was pumped and delivered separately to the three channels with diameters of 2 mm, 4 mm, and 6 mm. The sectional planes of reconstructed results are displayed in Fig. 6, and further details are shown in Table 2. Larger diameters were recorded in the reconstructed liquid flows compared to the real diameter values, in which 2 mm, 4 mm, and 6 mm enlarged to 4.43 mm, 5.64 mm, and 7.20 mm, respectively.

3.2. Reconstruction under different flow velocities

To simulate flow velocity of 21 cm/s, 31 cm/s, 41 cm/s and 51 cm/s as closely as possible, we set four speeds of flow, 20.33 cm/s, 29.67 cm/s, 38.91 cm/s, and 50.24 cm/s. The four velocities passed through the vascular channel of 4 mm, and the reconstructed results were presented in Fig. 7. The corresponding details are listed in Table 3. Notably, there was no significant change in reconstructed diameters under different flow velocities when comparing absolute error and ratio values.

In fact, two velocity scale settings (constant velocity scale and matched velocity scale) were employed using this set of velocities. In commercial ultrasound systems, alterations to the velocity scale setting may introduce changes to the pulse repetition frequency, thereby altering Doppler sensitivity. A constant velocity scale was set at the minimum velocity scale of the ultrasound device of 21 cm/s (the measuring scale in Table 3). In contrast, the matched velocity scale was used to adjust the measuring scale at 21 cm/s, 31 cm/s, 41 cm/s, and 51 cm/s to match the flow velocities. Under the constant velocity scale, it appeared that more bright areas could be identified, as depicted in the sectional planes in Fig. 8 (a). The comparison was also conducted by computing the ratios of the reconstructed diameter to the actual diameter, illustrated in Fig. 8 (b). These results indicated that the reconstructed diameter was larger under the constant velocity scale, while the matched velocity scale minimized the overrepresentation of diameter.

Table 2
The phantom channels under the velocity of around 50 cm/s (under 51 cm/s measuring scale).

Vascular channel (mm)	Flow speed (cm/s)	Reconstructed diameter (mm)	Absolute error (mm)	Ratio
2.00	52.78	4.43	2.43	2.21
4.00	50.24	5.64	1.64	1.41
6.00	50.26	7.20	1.20	1.20

3.3. Reconstruction under different depths from the ultrasound probe

The distance range from the temporal window to CoW was covered by setting up three depths of 3 cm, 6 cm, and 9 cm. The flow velocity was maintained at approximately 50 cm/s. All the parameter settings were kept constant with the gain adjusted for best displayed Doppler signal at depth of 9 cm. While scanning, a more pronounced color representation occurred when the vessel phantom was positioned closer to the ultrasound transducer. Additionally, a larger area of high flow velocity was observed in the middle color region (Fig. 9 (a)). A similar phenomenon was detected in the reconstructed objectives, as displayed in Fig. 9 (b). The size of the reconstructed fluid increased, and the flow velocity inside the fluid was elevated when the depth was closer to the probe. In this experiment, the start frame was also referred to as the start location. Fig. 9 (c) demonstrates the quantified diameter of the reconstructed vessels, with a higher ratio value recorded when the depth was closer to the probe.

The expansion of the reconstructed objectives might result from enlarged color areas. Given that the velocity scale setting could influence the size of the color area, we also examined the impact of color gain on this adjustment. The color gain was standardized for a depth of 9 cm, and adjustments were specifically made for 3 cm and 6 cm. The comparison of the ratio change is presented in Fig. 10 (a) and (b). Notably, a significant difference was consistently obtained between pre and post of adjustment, which were referred to as the matched and unmatched setting of color gain, respectively.

3.4. 3D CoW reconstructed from a human subject

The reconstructed CoW is presented in Fig. 11 (b). In contrast to the general reference of magnetic resonance angiography (MRA) in Fig. 11 (a), the vessels in the CoW could be distinguished in the reconstructed result, including ICAs, ACAs, partial MCA of the right side, and PCA connected with part of the basilar artery.

4. Discussion and conclusion

The aim of this study was to develop a novel 3D ultrasound imaging system and calculate its reconstructed accuracy when applied on brain vessels. To mimic cerebrovascular conditions, three variables were tested to validate the reconstructed resolution by calculating the absolute error and ratio of the reconstructed diameter in relation to the accurate diameter. The results showed that overrepresentation was

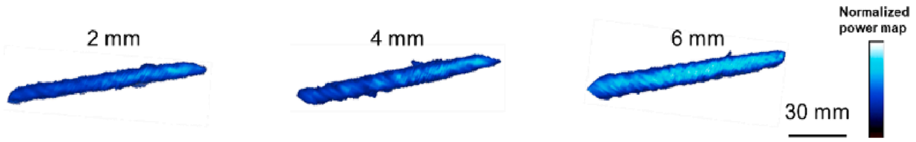

Fig. 6. The sectional planes of the reconstructed vascular channels with different diameters.

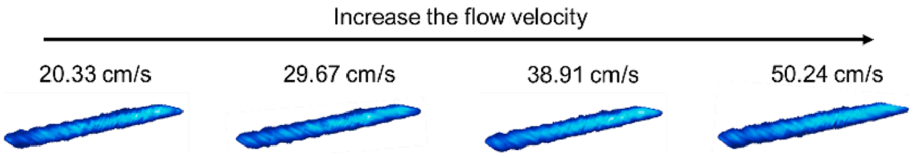

Fig. 7. The sectional planes of the reconstructed vascular channel (4 mm) with different flow velocities.

Table 3
The 4 mm channel under different flow velocities under 21 cm/s measuring scale.

Flow speed (cm/s)	Reconstructed diameter (mm)	Absolute error (mm)	Ratio
20.33	6.01	2.01	1.50
29.67	6.24	2.24	1.56
38.91	6.46	2.46	1.62
50.24	6.32	2.32	1.58

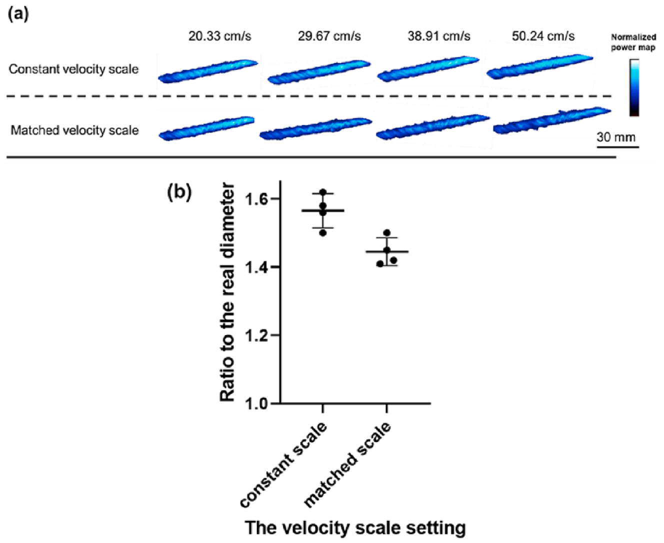

Fig. 8. (a) illustrates the sectional planes of the reconstructed objectives (4 mm channel). The planes were scanned under two velocity scale settings, constant velocity scale (fixed at 21 cm/s) and matched velocity scale (21 cm/s, 31 cm/s, 41 cm/s, and 51 cm/s). The flow velocities for the scanning were 20.33 cm/s, 29.67 cm/s, 38.91 cm/s, and 50.24 cm/s, respectively. (b) comparison between these two velocity scale settings in terms of the ratio of reconstructed diameter to the real diameter.

consistently detected in the reconstructed objectives. In contrast, higher values of absolute error and ratio were recorded in a smaller diameter channel, the 2 mm channel. This phenomenon may be caused by the higher internal pressure in the smaller vascular channel which would have pushed the channel walls of the elastic phantom outward. This explanation finds support in Barlow's formula ($P = 2St/D$). Since each channel in the phantom shared the same material property (S) and wall thickness (t), a smaller channel diameter (D) would result in higher internal pressure (P). Moreover, a relatively similar overrepresenting of reconstructed objectives was observed in different flow velocities, which did not exceed the Nyquist threshold because no aliasing or Nyquist effect occurred during data collection. It is likely that the size of the reconstructed flow may remain relatively constant if only the flow velocity in the Nyquist threshold is modified. For the different depths, the ratio values decreased as the depth increased. This may be caused by the size adjustment of the color window and change of interrogated depth because decreasing the size of the color window may enhance the temporal resolution and Doppler sensitivity. A significantly high interrogated depth decreases the amplitude of the Doppler signal [34]. As depicted in Fig. 9 (a), the system automatically adjusted to a smaller color window at a depth of 3 cm, enabling it to capture more Doppler information. Consequently, there was a greater availability of amplitude flow information detected at 3 cm in comparison to 6 cm and 9 cm depths. Meanwhile, we found that the setting of velocity scale influenced the size of the reconstructed flow because the values of ratio in matched scale group were lower than that of the constant scale group. Modifying the velocity scale can alter the PRF, with high velocity scale indicating a higher PRF but a less Doppler sensitivity [34]. Hence, more Doppler information was collected in the constant scale group, and this may have led to a larger reconstructed size. Regarding the color gain, it changed the size of the reconstructed flow by affecting the amplification of the Doppler signal [34]. Therefore, higher ratio values were recorded in the unmatched groups due to improper setting of color gain given that more noise components of the Doppler signal were included.

In mimicking the complexity of the CoW, the curvature of the vessel and realistically pulsated flow seem not to be considered in this study. In fact, we do not expect the curvature of a vessel to affect the result of 3D reconstruction, as flow in the curved vessel is still detectable in commercialized clinical ultrasound systems [40]. Regarding the realistically pulsated flow, the human volunteer will be in a comfortable

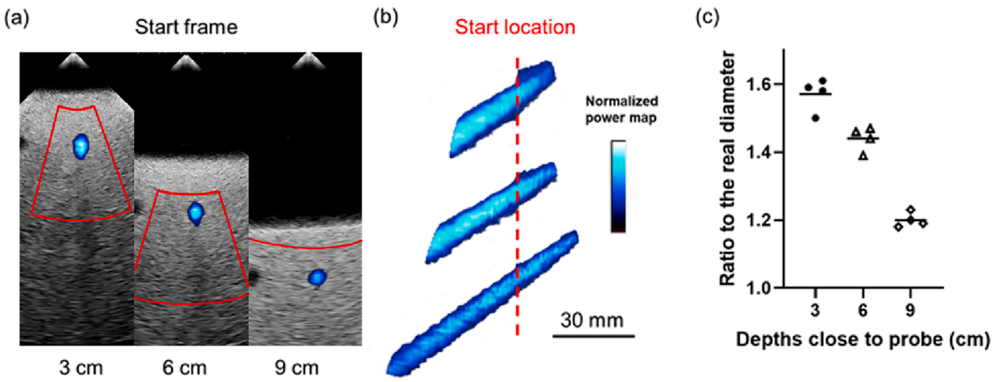

Fig. 9. (a) displays the starting frames of scanning at different depths. (b) indicates the sectional views of the reconstructed objectives measured at different depths, and here the start frame is referred to as the start location. (c) the comparison of the ratio values under different depths.

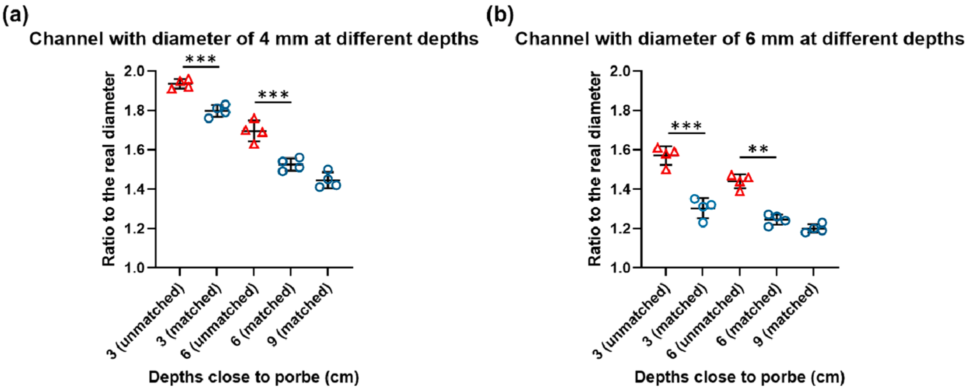

Fig. 10. The ratio values at different depths with the matched or unmatched setting of color gain. (a) the channel with a diameter of 4 mm. (b) the channel with a diameter of 6 mm. The red color represents “unmatched” and blue color represents “matched”. (For interpretation of the references to color in this figure legend, the reader is referred to the web version of this article.)

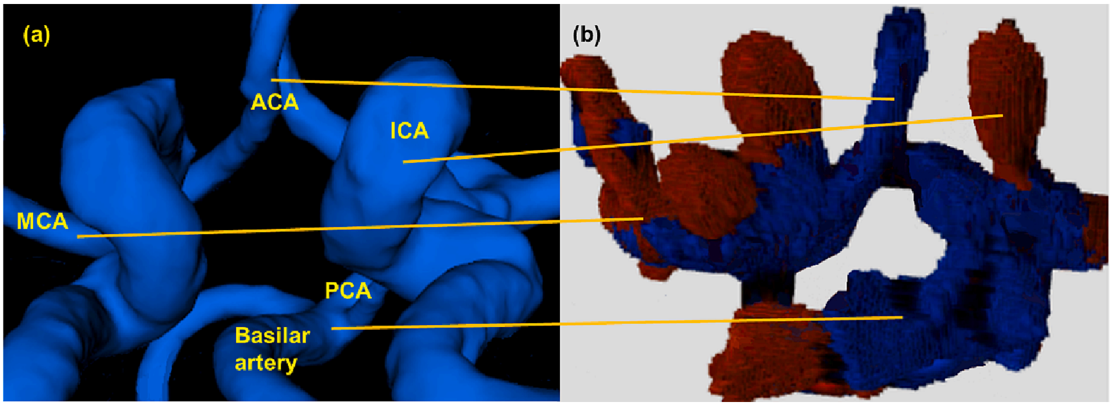

Fig. 11. (a) a general MRA reference indicating the location of the vessels in the CoW. (b) 3D reconstruction of the CoW on a human subject by images from the right side of the temporal window. ICA: internal carotid artery; MCA: middle cerebral artery; ACA: anterior cerebral artery; PCA: posterior cerebral artery.

resting state for data acquisition, so the peak systolic velocity will not vary a lot. The flow can thus be mimicked by a vessel phantom with constant flow velocity. Another important concept here is that ultrasound imaging is a linear system, in which output of a certain time point depends on the input of that time point only, but not on the input/output of a previous time point. This allows us to simplify the problem to constant flow and expand the results to describe pulsated flow. Since different cardiac phases would greatly affect the 3D image reconstruction, cardiac phase synchronization with the use of electrocardiology (ECG) signal will be used for future studies in human subjects.

In this investigation, it became evident that 3D ultrasound exhibits a limitation in achieving enlarged reconstructions compared to alternative imaging techniques like MRI and CT. This resulted in a relatively low accuracy in dimension measurements. However, it is possible that this limitation can be addressed by fine-tuning interdependent or independent factors, or by employing calibration techniques utilizing ratio values. Although the ratio values vary from device to device, they can be obtained through rigorous calculations. Hence, this study serves as a good reference for further studies on reconstruction of CoW or other related topics. In addition, no study has explored the effects of the setting of the wall filter. Amplitude or intensity of the flow may be affected by wall filter, also known as high-pass filter [34]. In this study, the setting of wall filter was not considered because there was no movement of vascular wall in the vessel phantom. Hence, the wall filter was set to a middle level to ensure a relatively low-flow state throughout all experiments. The present preliminary data has demonstrated the feasibility of using the 3D ultrasound imaging system on humans to reconstruct 3D CoW. The results are comparable to those of MRA visually. We are currently in the process of gathering both MRA and 3D ultrasound data from human subjects, and we plan to report the results in our upcoming publications, which will include a quantitative evaluation of vessel dimensions. The MRA will be used as a reference to guide the calibration of reconstruction on 3D transcranial color Doppler.

Declaration of competing interest

The authors declare that they have no known competing financial interests or personal relationships that could have appeared to influence the work reported in this paper.

Data availability

Data will be made available on request.

Acknowledgements

This study was partially supported by Hong Kong Innovation and Technology Commission [MRP/022/18X] and the Hong Kong Polytechnic University [ZE1Q]. Study design (SL, YPZ), data collection (SL, QTSS), data analysis (SL, YTL), writing (SL, QTSS, YTL), supervision (YPZ). All authors have read and approved the final submitted manuscript.

References

[1] V.L. Feigin, et al., Global, regional, and national burden of stroke and its risk factors, 1990–2019: a systematic analysis for the Global Burden of Disease Study

2019, Lancet Neurol. 20 (10) (2021) 795–820, https://doi.org/10.1016/S1474-4422(21)00252-0.

[2] Y.J. Wang, et al., “China stroke statistics, a report from the National center for healthcare quality management in neurological diseases, China national clinical research center for neurological diseases, the Chinese stroke association, National center for chronic and non-communicable disease control and prevention, Chinese center for disease control and prevention and Institute for global neuroscience and stroke collaborations,”, Stroke Vascul. Neurol. 5 (3) (2019) 2020, https://doi.org/10.1016/S1474-4422(21)00252-0.

[3] S.S. Virani, et al., Heart disease and stroke statistics—2021 update: a report from the American Heart Association, Circulation 143 (8) (2021) e254–e743, https://doi.org/10.1161/CIR.0000000000000950.

[4] E. S. Donkor and treatment, Stroke in the century: a snapshot of the burden, epidemiology, and quality of life, Stroke Res. Treat. vol. 2018, 2018. doi: 10.1155/2018/3238165.

[5] J.S. Balami, R. Chen, A.M. Buchan, Stroke syndromes and clinical management, QJM: An Int. J. Med. 106 (7) (2013) 607–615, https://doi.org/10.1093/qjmed/hct057.

[6] D.D. Cavalcanti, W. Feindel, J.T. Goodrich, T.F. Dagi, C.J. Prestigiacomo, M. C. Preul, Anatomy, technology, art, and culture: toward a realistic perspective of the brain, Neurosurg. Focus 27 (3) (2009) E2, https://doi.org/10.3171/2009.7.FOCUS09127.

[7] A. Chandra, W.A. Li, C.R. Stone, X. Geng, Y. Ding, The cerebral circulation and cerebrovascular disease I: Anatomy, Brain Circulat. 3 (2) (2017) 45, https://doi.org/10.4103/bc.bc_10_17.

[8] M.J. Krabbe-Hartkamp, et al., Circle of Willis: morphologic variation on three-dimensional time-of-flight MR angiograms, Radiology 207 (1) (1998) 103–111, https://doi.org/10.1148/radiology.207.1.9530305.

[9] R.A. Bergman, A.K. Afifi, R. Miyauchi, Circle of Willis,“ Illustrated Encyclopedia of Human Anatomic Variation: Opus II: Cardiovascular System: Arteries: Head, Neck, and Thorax, 2005. URL: https://www.anatomyatlases.org/AnatomicVariants/Cardiovascular/Text/Arteries/CircleofWillis.Shtml.

[10] Q. Li, J. Li, F. Lv, K. Li, T. Luo, P. Xie, A multidetector CT angiography study of variations in the circle of Willis in a Chinese population, J. Clin. Neurosci. 18 (3) (2011) 379–383, https://doi.org/10.1016/j.jocn.2010.07.137.

[11] M.A. Maaly, A.A. Ismail, Three dimensional magnetic resonance angiography of the circle of Willis: anatomical variations in general Egyptian population, Egypt. J. Radiol. Nucl. Med. 42 (3–4) (2011) 405–412, https://doi.org/10.1016/j.ejrnm.2011.09.001.

[12] K.D. Silva, R. Silva, W.L. Gunasekera, R.W. Jayesekera, Prevalence of typical circle of Willis and the variation in the anterior communicating artery: a study of a Sri Lankan population, Ann. Indian Acad. Neurol. 12 (3) (2009) 157, https://doi.org/10.4103/0972-2327.56314.

[13] G.N. David, O.R. Junior, Variations in the brain circulation: the circle of Willis, Braz. J. Morphol. Sci. (2012) 243–247.

[14] H. Riggs, C. Rupp, Variation in form of circle of Willis: the relation of the variations to collateral circulation: anatomic analysis, Arch. Neurol. 8 (1) (1963) 8–14, https://doi.org/10.1001/archneur.1963.00460010024002.

[15] K. Kapoor, B. Singh, I.J. Dewan, Variations in the configuration of the circle of Willis, Anat. Sci. Int. 83 (2) (2008) 96–106, https://doi.org/10.1111/j.1447-073X.2007.00216.x.

[16] B. Eftekhar, M. Dadmehr, S. Ansari, M. Ghodsi, B. Nazparvar, E. Ketabchi, Are the distributions of variations of circle of Willis different in different populations? – Results of an anatomical study and review of literature, BMC Neurol. 6 (1) (2006) 1–9, https://doi.org/10.1186/1471-2377-6-22.

[17] Z. Vrselja, H. Brkic, S. Mrdenovic, R. Radic, G. Curic, Function of circle of Willis, J. Cereb. Blood Flow Metab. 34 (4) (2014) 578–584, https://doi.org/10.1038/jcbfm.2014.7.

[18] P.V. Banga, et al., Incomplete circle of Willis is associated with a higher incidence of neurologic events during carotid eversion endarterectomy without shunting, J. Vasc. Surg. 68 (6) (2018) 1764–1771, https://doi.org/10.1016/j.jvs.2018.03.429.

[19] D. Caro, et al., Variants of the circle of Willis in ischemic stroke patients, J. Neurol. 268 (10) (2021) 3799–3807, https://doi.org/10.1007/s00415-021-10454-4.

[20] C. Zhou, et al., Association between incomplete circle of willis and carotid vulnerable atherosclerotic plaques: a Chinese atherosclerosis risk evaluation study, Arterioscler. Thromb. Vasc. Biol. 38 (11) (2018) 2744–2749, https://doi.org/10.1161/ATVBAHA.118.311797.

[21] T.V. Seeters, et al., Completeness of the circle of Willis and risk of ischemic stroke in patients without cerebrovascular disease, Neuroradiology 57 (12) (2015) 1247–1251, https://doi.org/10.1007/s00234-015-1589-2.

[22] M.M. Lell, J.E. Wildberger, H. Alkadhi, J. Damilakis, M. Kachelriess, Evolution in computed tomography: the battle for speed and dose, Invest. Radiol. 50 (9) (2015) 629–644, https://doi.org/10.1007/s00234-015-1589-2.

[23] M.S. Davenport, et al., Use of intravenous iodinated contrast media in patients with kidney disease: consensus statements from the American College of Radiology and the National Kidney Foundation, Kidney Medicine 2 (1) (2020) 85–93, https://doi.org/10.1148/radiol.2019192094.

[24] R.R. Edelman, I. Koktzoglou, Noncontrast MR angiography: an update, J. Magn. Reson. Imaging 49 (2) (2019) 355–373, https://doi.org/10.1002/jmri.26288.

[25] J. Carrizosa, Transcranial Doppler (TCD/TCCS) Approaches: Acoustic Windows, in: Neurosonology in Critical Care: Monitoring the Neurological Impact of the Critical Pathology, pp. 177-194, 2021. doi: 10.1007/978-3-030-81419-9_10.

[26] T.L. Szabi, Chapter 11 - Doppler Modes, Diagnostic Ultrasound Imaging: Inside Out (Second Edition), pp. 431-500, 2014. doi: 10.1016/B978-0-12-396487-8.00011-2.

[27] Q. Huang, Z. Zeng, A review on real-time 3D ultrasound imaging technology, BioMed Res. Int. 2017 (2017). doi: 10.1155/2017/6027029.

[28] A. Delcker, B. Turowski, Diagnostic value of three-dimensional transcranial contrast duplex sonography, J. Neuroimaging 7 (3) (1997) 139–144, https://doi.org/10.1111/jon199773139.

[29] C. Klötzsch, A. Bozzato, G. Lammers, M. Mull, J. Noth, Contrast-enhanced three-dimensional transcranial color-coded sonography of intracranial stenoses, Am. J. Neuroradiol. 23 (2) (2002) 208–212.

[30] A. Bauer, U. Bogdahn, A. Haase, R. Schlief, 3-Dimensional echo-enhanced transcranial Doppler ultrasound diagnosis, Radiologe 38 (5) (1998) 394–398, https://doi.org/10.1007/s001170050370.

[31] C. Klotzsch, A. Bozzato, G. Lammers, M. Mull, B. Lennartz, J. Noth, Three-dimensional transcranial color-coded sonography of cerebral aneurysms, Stroke 30 (11) (1999) 2285–2290, https://doi.org/10.1161/01.STR.30.11.2285.

[32] B.D. Lindsey et al., The ultrasound brain helmet for 3D transcranial Doppler imaging, in: 2009 IEEE International Ultrasonics Symposium, 2009: IEEE, pp. 1395-1398. doi: 10.1109/ULTSYM.2009.5441617.

[33] N.M. Ivancevich, G.F. Pinton, H.A. Nicoletto, E. Bennett, D.T. Laskowitz, S. W. Smith, Real-time 3-D contrast-enhanced transcranial ultrasound and aberration correction, Ultrasound Med. Biol. 34 (9) (2008) 1387–1395, https://doi.org/10.1016/j.ultrasmedbio.2008.01.015.

[34] D. Maulik, Sonographic color flow mapping: basic principles, In: Doppler Ultrasound in Obstetrics and Gynecology, 2005, pp. 69-84. doi: 10.1007/3-540-28903-8_6.

[35] P. Hoskins, A. Criton, Colour flow, power Doppler and tissue imaging, Diagnostic Ultrasound: Physics and Equipment (Second Edition), pp.121–141, 2010. URL: https://dl.icdst.org/pdfs/files3/08e853dc7f6b4fd4b5a3cc6fccde7b2f.pdf.

[36] A.T. Rai, J.P. Hogg, B. Cline, G.J.J.o.n.s. Hobbs, Cerebrovascular geometry in the anterior circulation: an analysis of diameter, length and the vessel taper, J. Neurointervent. Surg. 5(4) (2013) 371-375. doi: 10.1136/neurintsurg-2012-010314.

[37] R. Aaslid, T. Markwalder, H. Nornes, Noninvasive transcranial Doppler ultrasound recording of flow velocity in basal cerebral arteries, J. Neurosurg. 57 (6) (1982) 769–774, https://doi.org/10.3171/jns.1982.57.6.0769.

[38] M. Hennerici, W. Rautenberg, G. Sitzer, A. Schwartz, Transcranial Doppler ultrasound for the assessment of intracranial arterial flow velocity—Part 1. Examination technique and normal values, Surg. Neurol. 27 (5) (1987) 439–448, https://doi.org/10.1016/0090-3019(87)90251-5.

[39] A.V. Alexandrov, et al., Practice standards for transcranial Doppler ultrasound: part I—test performance, J. Neuroimaging 17 (1) (2007) 11–18, https://doi.org/10.1111/j.1552-6569.2006.00088.x.

[40] C. Deane, Chapter on Doppler ultrasound: principles and practice,“ Doppler in Obstetrics, URL:https://fetalmedicine.org/var/uploads/web/Doppler/Doppler%20Ultrasound%20-%20Principles%20and%20practice.pdf.